Integration of binocular vision and motor state to promote prey pursuit

Authors

Guangnan Tian[1]† Thomas Ka Chung Lam[2]‡† Gewei Yan[3]† Yingzhu He[3], Biswadeep Khan[2], Jianan Y. Qu[3]*, Julie L. Semmelhack[1,2]*

Affiliations

[1]Division of Life Science, The Hong Kong University of Science and Technology, Clear Water Bay, Kowloon, Hong Kong S.A.R., China
[2]Department of Chemical and Biological Engineering, The Hong Kong University of Science and Technology, Clear Water Bay, Kowloon, Hong Kong S.A.R., China
[3]Department of Electronic and Computer Engineering, The Hong Kong University of Science and Technology, Clear Water Bay, Kowloon, Hong Kong S.A.R., China
‡ Current address: Neuroengineering Laboratory, Brain Mind Institute & Interfaculty Institute of Bioengineering, EPFL, Lausanne, Switzerland
†These authors contributed equally: Guangnan Tian, Thomas Ka Chung Lam, Gewei Yan
*Correspondence: Julie L. Semmelhack jsemmelhack@ust.hk and Jianan Y. Qu eequ@ust.hk

Abstract

Most animals with two eyes combine the inputs to achieve binocular vision, which can serve numerous functions, and is particularly useful in hunting prey. However, the mechanisms by which visual information from the two eyes are combined remain largely unknown. To address this question, we identified the binocular neurons that respond to prey in zebrafish (bino-PRNs). These neurons respond specifically to prey, and their activity is enhanced during hunting. To explore the relationship between bino-PRNs and hunting, we optogenetically induced hunting and found that the bino-PRNs receive excitatory input during hunting. To determine the role of the bino-PRNs in behavior, we optogenetically activated them, and found that they promote forward prey capture swims. Our results support a model where bino-PRNs integrate sensory information from the two eyes with hunting state information to drive approach toward prey in the binocular zone.

Introduction

All animals with binocular vision must integrate the two eyes' signals to produce a unified percept and behavioral response, and this integration should occur in binocular neurons which receive input from both eyes. Binocular neurons in the visual cortex have been identified in non-human primates as well as mice, but it remains unclear where and how the inputs are first combined(*1, 2*). One proposed driver of the evolution of binocular vision is predation(*3*), and binocular vision has been proposed to play a key role in hunting in a diverse range of animals, from insects to cephalopods to mice(*4–6*). Mice have been shown to place prey objects in their binocular visual field, and ipsilateral retinal ganglion cell input is important for hunting(*7*). However, it has been difficult to identify the binocular neurons that respond to the prey during hunting episodes, and to manipulate these neurons to determine their role in hunting behavior.

Binocular vision is also thought to play a key role in zebrafish hunting behavior. Zebrafish larvae have laterally positioned eyes that normally have little binocular overlap, but the eye convergence at the beginning of a hunting episode creates a binocular zone(*8*). Although binocular interactions have been identified in the context of whole-field motion and luminance stimuli(*9–11*), so far, binocular prey-responsive neurons have not been identified.

Zebrafish prey capture is typically initiated by the entry of a paramecium or other small moving object into the peripheral visual field. In response to this stimulus, the larva converges its eyes and hooks its tail in a J shape to turn toward the prey. These actions bring the prey from the peripheral to the central visual field,(*8, 12–15*) after which the larva may then perform a more symmetrical forward swim to approach the prey, before executing a capture strike to consume it(*12, 14*). After the initial J-turn and eye convergence, the prey stimulus can be seen by both eyes, and larvae could potentially use the binocular input to estimate prey distance or azimuth, or to improve prey detection(*16*).

Prey is first detected by retinal ganglion cells which project to the pretectum (Pt) and optic tectum (OT)(*17*), and prey stimuli have been shown to activate neurons in the Pt, OT and thalamus (Thal)(*18*). In addition, neurons within the Pt have been shown to induce hunting behavior via output to the hindbrain tegmentum, suggesting that they constitute a command system for hunting(*18*). However, it is unclear if and where the prey inputs from the two eyes are combined to produce binocular neurons, and what functions these neurons might serve in prey capture behavior.

Here, we describe a population of binocular neurons in the Pt, Thal and nucleus isthmi (NI) that is activated by prey input from either eye (bino-PRNs) and further enhanced by hunting. We identified a Gal4 line with a large proportion of bino-PRNs, and found that hunting triggered by activation of command-like hunting neurons activates neurons in this line, suggesting that the bino-PRNs are downstream of the hunting motor command. Finally, we optogenetically activated these neurons in conjunction with the command neurons, and found that they bias the larvae toward more symmetrical prey capture forward swims that occur later in the prey capture motor sequence. These results suggest that bino-PRNs integrate sensory input from both eyes as well as the prey capture motor signal, to drive approach toward the prey.

Results

Eye-blocker reversibly blocks input to one eye

To identify binocular prey-responsive neurons, we designed and 3D-printed a device to block one or both eyes selectively and reversibly by laterally moving its arms in front of the eyes (Figs. 1A and 1B). The larvae were embedded in agarose with the tail free, and although the eyes were fixed, we could observe eye convergences of a few degrees in response to UV prey stimuli. In order to restrict the prey stimulus to a small part of the visual field, we designed a circulating

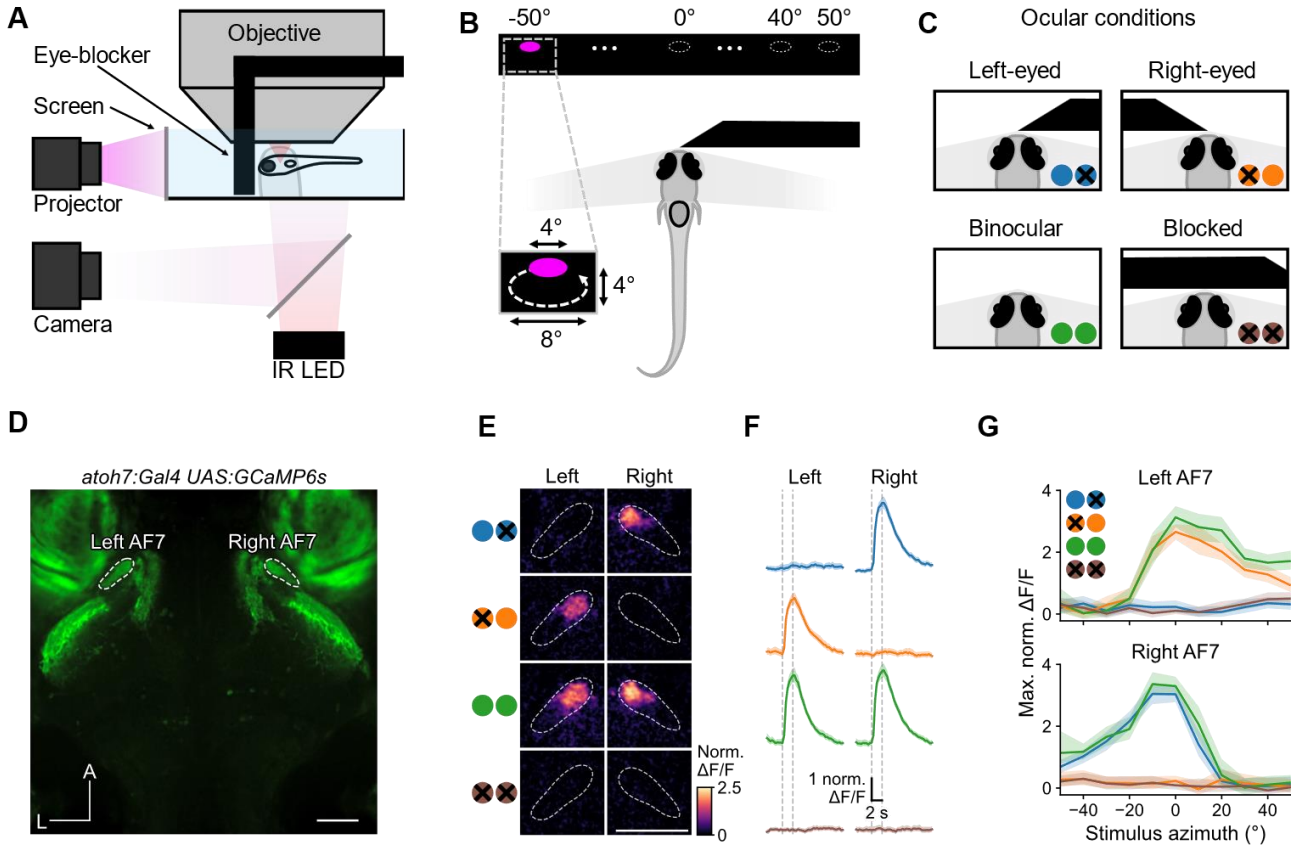

Fig. 1. Reversible occlusion of one eye blocks the response to prey stimuli. (A) Schematic of the experimental setup: the eye-blocker is positioned in front of the fish to block visual input. **(B)** Bright UV circulating prey-like stimuli were presented at azimuths from -50° (left) to +50° (right). **(C)** Larvae were tested under 4 ocular conditions: right eye blocked, left eye blocked, neither eye blocked and both eyes blocked. **(D)** Baseline fluorescence image showing AF7s labelled with GCaMP6s (Scale bar, 50 µm). **(E)** Activation of AF7 in left eye, right eye, binocular, and fully blocked conditions in one example larva (Scale bar, 50 µm). Pixels are color-coded by trial-averaged increase in mean ΔF/F during the stimulus interval compared to that during the 2 s before the stimulus. **(F)** Response of the left and right AF7 to 0° prey stimulus. Vertical dashed lines indicate the stimulus interval. Solid line and shaded region represent the mean and 95% confidence interval, respectively (n = 7 fish). **(G)** Spatial tuning curves showing maximum activity of AF7 (within the 3 s time window after stimulus onset) in response to prey stimuli at different azimuths. Solid lines and shaded regions represent the mean and 95% confidence interval, respectively (n = 7 fish).

stimulus which moved through an 8°×4° elliptical track, and presented this stimulus at a range of azimuths from -50° (left) to 50° (right) of the visual field (Fig. 1B). We moved the eye-blocker to different positions between prey presentations such that all stimuli were presented during all four ocular conditions: left eye exposed (left-eyed), right eye exposed (right-eyed), both eyes exposed (binocular), and both eyes blocked (blocked) (Fig. 1C). We tested the completeness of the block by recording visual responses in arborization field 7 (AF7), a retinorecipient region that responds to prey stimuli(*17*), and found that, as expected, blocking one eye completely blocked the input to AF7 in the hemisphere contralateral to that eye (Figs. 1D and 1E). This pattern was consistent across 7 fish (Fig. 1F) and held true for all the stimulus azimuths (Fig. 1G).

We also found that blocking one eye affected the range of azimuths that would trigger hunting, and the kinematics of the prey capture swims. In the monocular condition, larvae would respond to prey on the exposed eye side, and up to 10° on the blocked side, not to more lateral stimuli on the blocked side, indicating that the binocular field in our eyes-fixed condition is +/- 10° (Fig. S1A). For central prey stimuli, the occlusion also caused larvae to bias the initial hunting tail beat to the exposed eye side (Fig. S1B), and bout asymmetry (a measure of "J-ness", or time the curvature of the distal part of the tail matched the overall bout direction) was higher in the monocular conditions (Fig. S1C), indicating that the presence of the blocker affected hunting behavior.

One population of prey responsive neurons is binocular

We next used two-photon imaging to identify prey-responsive neurons (PRNs) in binocular and monocular conditions. We used an electrically tunable lens to image a 500×500×100 μm volume which included the OT, Pt, tegmentum (Teg), nucleus isthmi (NI), and thalamus (Thal) (Fig. 2A). All these areas have previously been shown to respond to prey stimuli(*18–23*). For larvae expressing nuclear-localized GCaMP6s pan-neuronally (*Tg(elavl3:Hsa.H2B-GCaMP6s)jf5Tg*, aka *elavl3*)(*24*), we presented the same visual stimuli as in Fig. 1 while recording calcium responses in 9 planes of the brain at 3 volumes per second, and mapped the positions of the cell bodies onto the mapZebrain atlas(*25*) (Fig. S2A). We moved the eye-blocker to different positions with respect to the larva to record the response to each stimulus in the left-eyed, right-eyed, binocular, and fully blocked conditions (Figs. 2B and 2C). We also recorded eye and tail movements, and used eye convergence as a marker for hunting (Fig. 2D, Movie S1). To identify PRNs, we modeled the activity of each neuron as a weighted sum of stimulus regressors (Fig. S2B). We found that neurons with $R^2 \geq 0.3$ were well correlated with prey stimuli (Fig. S2C), and that the fully blocked condition resulted in virtually no PRNs above this threshold (Fig. S2D). Therefore, we defined neurons with $R^2 \geq 0.3$ as prey responsive. We then used spatial p-value analysis(*26*) to remove neurons that were not colocalized across the 15 fish. We found that, while the majority of the responsive neurons were in the hemisphere contralateral to the unblocked eye, we also observed a smaller population of PRNs in the hemisphere ipsilateral to the unblocked eye, and we termed these neurons "ipsi-neurons" (Fig. 2E). To confirm that the ipsi-neurons are not an artifact of incomplete eye occlusion, we also performed lensectomies to remove one lens of the larvae, which renders larvae unable to respond to prey(*14*) (Fig. S3A). The PRN patterns of sham, unilateral and bilateral delensed fish resembled those produced by the eye-blocker, and ipsi-neurons were found in the Pt, Thal and NI of unilaterally delensed larvae (Figs. S3B and S3C).

We next asked how the population of PRNs responded across different ocular conditions; for example, whether a particular PRN could respond to input from either eye (Fig. 2F). As expected, a large class of PRNs only responded to contralateral eye input, and failed to respond to ipsilateral input (mono-contra, Fig. 2G). We also found that a small population within the ipsi-neurons was unresponsive to contralateral eye input (mono-ipsi, Fig. S2E). Finally, one population of ipsi neurons also responded to input from the contralateral eye, meaning that either

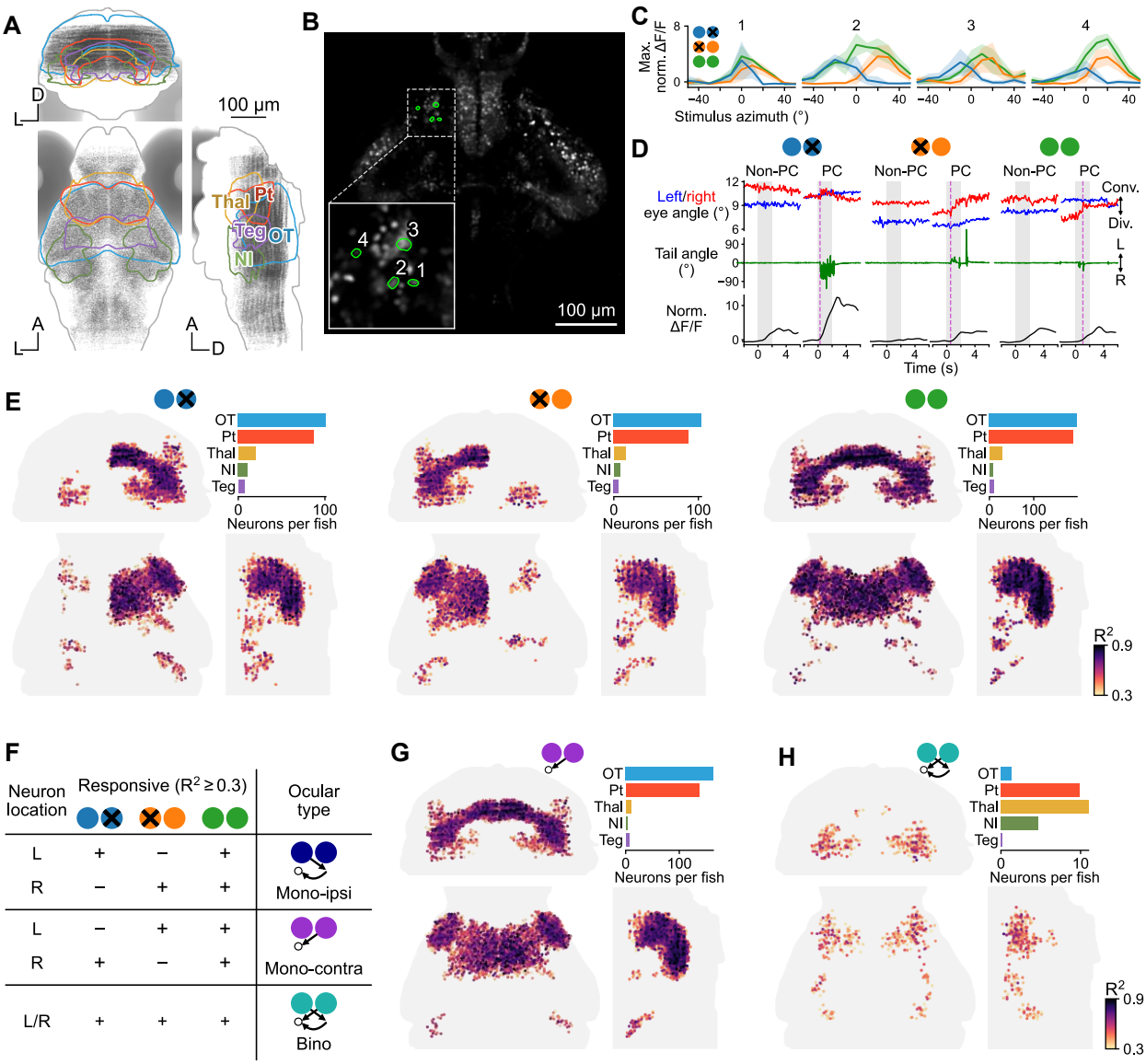

Fig. 2. Volumetric two photon imaging in different ocular conditions identifies binocular prey-responsive neurons (PRNs). (A) Map of the imaging volume. Each grey dot represents one neuron. Coronal, horizontal and sagittal views (all anatomical maps follow the same layout unless otherwise stated). **(B)** Example PRNs in Pt. **(C)** Maximum activity (within the 3 s time window after stimulus onset) of each neuron in response to stimuli at different azimuths in the three ocular conditions. Solid lines and shaded regions represent mean and ±1 SD, respectively (n = 8 trials). **(D)** Eye and tail movements triggered by prey stimuli and normalized ΔF/F responses of example neuron no. 1. Magenta dashed lines indicate hunting onsets (defined by eye convergence). **(E)** Maps of PRNs in different ocular conditions from coronal, horizontal, and sagittal views (n = 15 fish). Neurons with prey-related activity were identified with regression analysis for each ocular condition, using an R^2 threshold of 0.3. Color code represents R^2 value. Bar plots show average number of neurons in selected brain regions. **(F)** Schematic of the assignment of ocular type based on responsiveness in different ocular conditions. **(G-H)** Maps of the anatomical locations of monocular contra PRNs (mono-contra) and binocular PRNs (bino-PRNs).

eye could activate them (binocular, Fig. 2H). We identified the anatomical locations of the binocular PRNs (bino-PRNs), and found that they were predominantly mapped to three areas: the Pt, Thal, and NI (Fig. 2H, bar plot).

Bino-PRNs respond specifically to prey-like stimuli and show enhanced activity during hunting trials.

Next, we investigated whether bino-PRNs respond specifically to prey, or are activated by other types of stimuli. As zebrafish primarily use red cones to detect global motion(*27, 28*), we introduced a red background to all visual stimuli in the section. Zebrafish larvae were first presented with circulating prey dots as in Fig. 2, and then with a battery of eight additional stimuli (darkening/brightening, sweeping UV dots, horizontally moving gratings, and looming disks) in the binocular condition (Fig. S4A).

We identified bino- and mono-PRNs as in Fig. 2 (Fig. S4B). Using affinity propagation clustering followed by hierarchical clustering(*22*), neurons were grouped into functional types according to their responses to the eight visual stimuli (Fig. S4C). The vast majority of bino-PRNs were assigned to cluster 2 (Figs. S4D and S4E), which responded to both leftwards and rightwards moving dots (Fig. S4F). In summary, bino-PRNs respond selectively to prey-like stimuli moving in both horizontal directions.

Bino-PRNs appeared in some cases to respond more robustly in hunting trials than non-hunting trials (Fig. 2D), and to further investigate this property, we plotted the responses of bino-PRNs in each brain region (Fig. S5A) in prey capture (PC) vs. non-prey capture (non-PC) trials. Indeed, the bino-PRNs in each area were on average more activated in prey capture trials (Fig. S5B). Thus, one possibility could be that these neurons are binocular as a result of receiving a motor signal, rather than visual input from both eyes. However, their binocularity was not entirely a result of the hunting state, as they were activated by prey stimuli seen by the ipsilateral eye even in non-hunting trials (Fig. S5B, middle column, black lines). In contrast, the contra-PRNs in the OT, which constitute the majority of the PRN population, had no response to ipsilateral prey, even in hunting trials (Fig. S5B, lowest row). This suggests that the bino-PRNs are receiving sensory input from both eyes, as well as responding more strongly in hunting trials.

Bino-PRNs are activated by prey sensory input to either eye across the visual field and the non-sensory component of their response is correlated with hunting.

To further investigate the functional properties of the binocular neurons, we clustered the PRNs based on their coefficients from a multiple linear regression analysis. This model includes sensory regressors for each combination of stimulus azimuth and ocular condition, along with motor regressors representing the strength of prey capture movements to the left and right. Instead of directly using motor regressors convolving prey capture bouts to the left (PC_L) or right (PC_R), we selected for neurons most correlated to either of the two regressors to act as motor seeds. We used motor seed neuron average activity as the model regressors, reasoning that using real neural activity would be more realistic(*29*) (Fig. S6A). We identified sets of Pt and hindbrain neurons that were correlated with prey capture (PC) bouts (Fig. S6B, red lines). These neurons didn't respond to spontaneous swims (Fig. S6B, black lines). Since the hindbrain neurons responded only in the prey capture (PC) trials while Pt neurons responded to prey stimuli in the non-prey capture (non-PC) trials (Fig. S6C), we used the hindbrain neurons as the motor seeds. We then performed multiple linear regression analysis and used t-SNE dimensionality reduction and K-means clustering to delineate sensorimotor PRN clusters (Fig. 3A). We found that several (1-8) seemed to be sensory clusters, and responded to prey stimuli at multiple azimuths with a Gaussian-like tuning curve, such that they cover the full range of azimuths we tested (Fig. 3B, orange, blue and green lines). These clusters were only slightly modulated by hunting responses

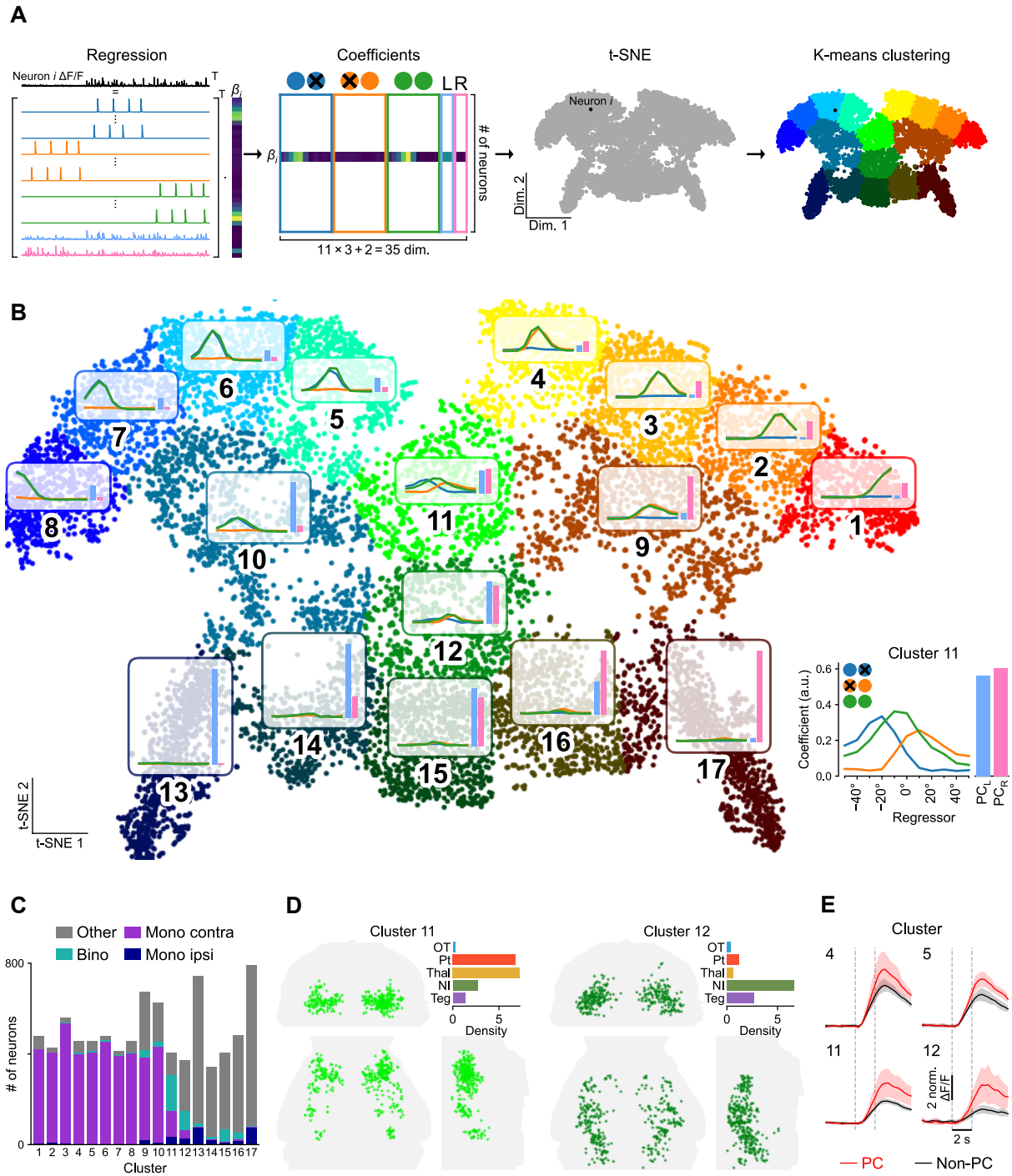

Fig. 3. PRNs form clusters with varying sensorimotor properties, with bino-PRNs in two motor-correlated clusters. (A) Schematic of functional clustering pipeline. Neural activity was analyzed by multivariate linear regression with 35 regressors (11 azimuths × 3 ocular conditions + 2 motor regressors). PRNs were defined as neurons with $R^2 \geq 0.3$. The 35-dimensional coefficient vectors were embedded in a 2D space using t-SNE. K-means clustering was then applied to these 2D data points, resulting in the identification of 17 distinct clusters. **(B)** PRNs formed 17 clusters with varying sensorimotor properties. Insets show sensory (blue, green and orange lines) and motor (teal and pink bars) coefficients. **(C)** Number of bino- and mono-PRNs in each cluster. **(D)** Anatomical locations of neurons in clusters 11 and 12. **(E)** Average response of clusters 4, 5, 11 and 12 in prey capture (PC) and non prey capture (non-PC) trials. Shaded regions represent ±1 SD. n = 15 fish.

(Fig. 3B, teal and pink bars). Anatomically, the neurons in these clusters were predominantly located in the OT (Fig. S7), which is consistent with previous findings of a spatial map for prey responses in the tectum(*30*). However, the clusters which were activated by stimuli in the central visual field (clusters 3-6, Fig. S7) also had a substantial number of pretectal neurons.

In addition, we also identified several clusters that were more modulated by hunting and could therefore be candidates to receive motor-related signals (Fig. 3B, clusters 9-17). Four clusters showed both sensory and motor tuning (clusters 9-12). Two of these clusters were modulated by unidirectional hunting responses: to the right (cluster 9) and left (cluster 10), and only responded to contralateral eye sensory input (Fig. 3b). Two others, clusters 11 and 12, were modulated by hunting in either direction and were responsive to visual input from both eyes (Fig. 3B). Finally, the bottom row of clusters were highly modulated by hunting but not tuned to any particular sensory regressor (Fig. 3B, clusters 13-17). These neurons were located primarily in the NI and hindbrain (Fig. S7).

To investigate which clusters contain the bino-PRNs, we plotted how the neurons were distributed into the four ocular types (binocular, monocular ipsi and monocular contra) for each of the 17 clusters. Interestingly, none of the sensory clusters (1-8) had a significant proportion of bino-PRNs (Fig. 3C). Clusters 1-10 consisted of mostly contra-PRNs, while clusters 11 and 12 contained the majority of the bino-PRNs (Fig. 3C, cyan). The difference between these clusters seems to be that cluster 11 is more sensory-tuned, while cluster 12 is more motor-tuned (Fig. 3B). We then plotted the anatomical locations of the neurons in these clusters, and found that they were located in the Pt, Thal and NI in the case of cluster 11, and primarily in the NI in the case of cluster 12 (Fig. 3D). We plotted the average response of these two clusters in go and no-go trials, and in comparison to the monocular clusters 4 and 5, clusters 11 and 12 were indeed significantly more motor-modulated (Fig. 3E) This suggests that the bino-PRNs may either generate or receive the hunting motor signal.

The *lhx9:Gal4* line labels bino-PRNs.

We next sought to identify Gal4 lines labeling the bino-PRNs to allow us to use a genetic marker to image and manipulate these neurons. We therefore performed functional imaging of several lines in different ocular conditions. We first tested the *KalTA4u508* line, which was reported to express KalTA (a Gal4 variant) in the hunting command-like neurons of the accessory pretectal nucleus (APN) (Fig. 4A)(*18*). It is possible that these command-like neurons could be integrating input from the two eyes. However, when we imaged *Tg(KalTA4u508;UAS:GCaMP6s)* larvae, we found that almost all PRNs were responsive only to the contralateral eye prey stimulation, and were classified as mono-ipsi or mono-contra (Figs. 4B-D and 4I). All of the pretectal PRNs in the line were mono-contra, meaning that the pretectal command-like neurons must be receiving input from only the contralateral eye.

In contrast, when we imaged *Tg(lhx9:Gal4;UAS:GCaMP6s)* larvae(*31*) (Fig. 4E), we found that the majority of PRNs were binocular. The *lhx9+* bino-PRNs were located in the Pt (as well as Thal) and the anterior parts of the NI (aNI) (Figs. 4F-H). These neurons were activated by prey presented to either the contra- or ipsilateral eye (Fig. 4J). Indeed, these neurons were activated by ipsilateral prey even in the absence of hunting, similar to the bino-PRNs in the panneuronal dataset (Fig. S5). Taken together, these data suggest that the *lhx9+* bino-PRNs represent a separate population that is not labelled by the *KalTA4u508* line. We can therefore use these two lines to investigate the source of the motor enhancement of the bino-PRNs.

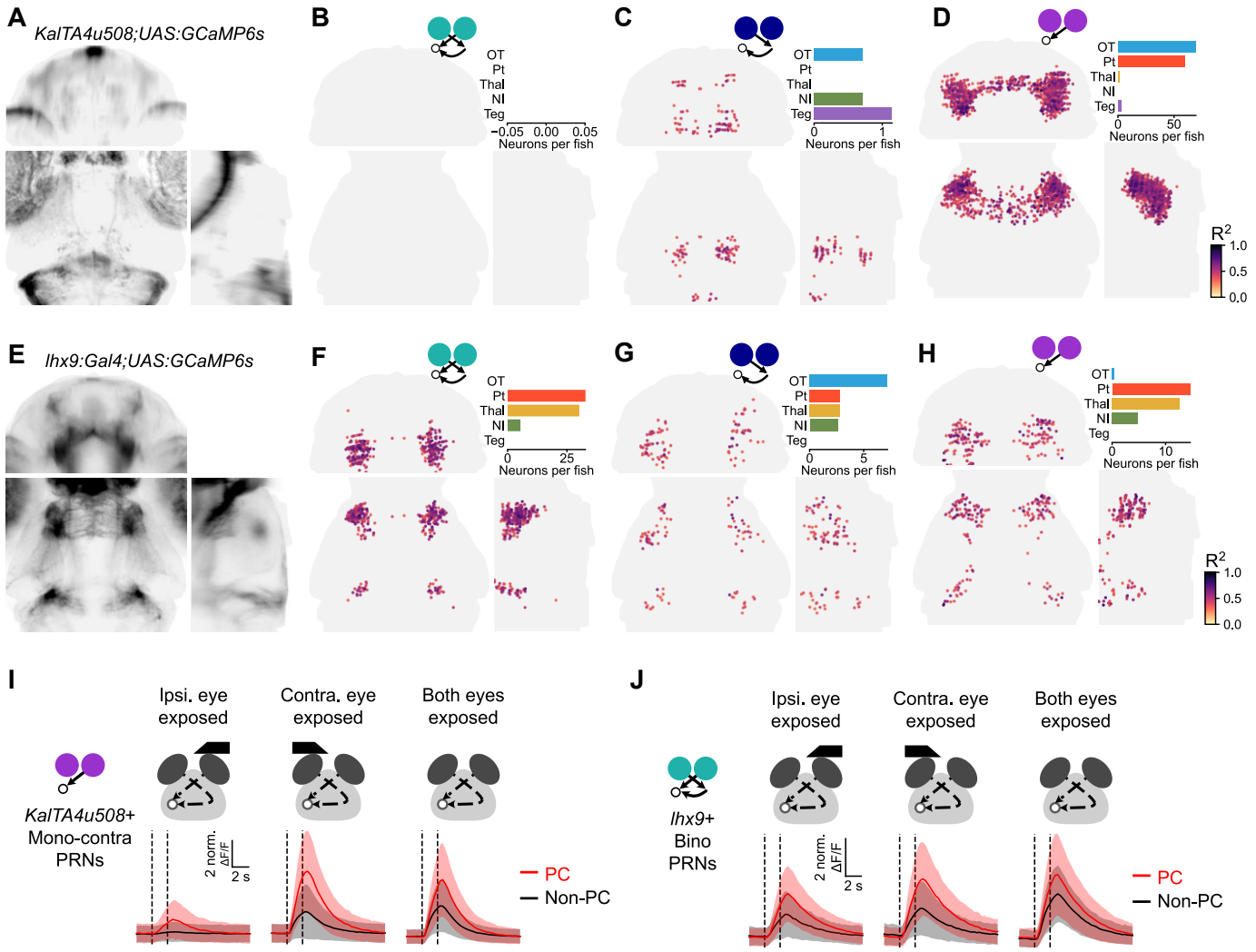

Fig. 4. Identification of a transgenic line labelling bino-PRNs. (A) Expression pattern of the *KalTAu508* line. **(B,C,D)** Binocular, mono-ipsi and mono-contra PRNs in the *u508* line (n = 7 fish). **(E)** Expression pattern of the *lhx9* line. **(F,G,H)** Binocular, mono-ipsi and mono-contra PRNs in the *lhx9* line (n = 5 fish). **(I)** Average response of the mono-contra PRNs in the *KalTA4u508* line in prey capture (PC) and non prey capture (non-PC) trials. Solid lines and shaded regions represent mean and ±1 SD, respectively. **(J)** Average response of the bino-PRNs in the *lhx9* line. Solid lines and shaded regions represent mean and ±1 SD, respectively.

Optogenetically triggered hunting events activate *lhx9+* Pt, Thal and NI neurons in the absence of prey.

Based on the enhanced activity of bino-PRNs in hunting trials (Fig. S5), we hypothesized that they could be activated as a consequence of hunting. Zebrafish larvae normally have unconverged eyes, to maximize coverage of the visual field, and only converge their eyes at the onset of a hunting episode(*8, 12, 15*). It may be that in order for the brain to properly interpret visual input, some information about convergence/hunting state has to be conveyed to visual areas. One way for this information to get there would be via corollary discharge, or an internal signal that is the result of a motor command(*32*). In this case, visual areas, and specifically bino-PRNs, could receive a signal that is the result of the hunting motor command, that would indicate that the eyes are converged, and the animal is hunting. This information could be important for localizing prey in space, or it could be a predictive signal that increases the sensitivity to prey in the region of the visual field where it is expected to be after convergence(*33, 34*).

If bino-PRNs receive a hunting corollary discharge, we would predict that when hunting is induced by artificial stimulation of the command-like neurons, bino-PRNs would also be activated (Fig. 5A). We therefore asked whether optogenetic activation of *KalTA4u508* APN neurons would activate the *lhx9* line, which primarily contains bino-PRNs (Fig. 4F). We expressed GCaMP6s and Channelrhodopsin (ChR2) in the *u508* and *lhx9+* neurons (*Tg(KalTA4u508;lhx9Gal4;UAS-GCaMP6s;UAS:ChR2(H134R)-mCherry)* larvae). We used 920 nm 2-photon 3D-holographic stimulation to activate a small area (12 x 12 µm) within the APN of these larvae. At the same time, we imaged GCaMP at 1020 nm (Fig. 5B, left)(*35*). The optogenetic sessions were followed by a visual stimulation session, in which the fish was presented with prey-like stimuli (Fig. 5B, right). We used eye convergence to define hunting events, and found that these events occurred during the optogenetic experiments, both in and out of phase with the holographic stimulation (Figs. 5C, middle panel, red dashed lines, and S8A). These bouts were characterized by eye convergence and J-turn or forward swim tail movements (Fig. S8B).

To determine whether these hunting bouts were due to the two-photon scanning activating ChR2, we performed control experiments in larvae with different combinations of the three transgenes. We found that the ChR2 and *KalTA4u508* transgenes were essential for the induction of hunting (Fig. S8C). In fish carrying these two transgenes, we did observe hunting bouts in experiments with scanning but no stimulation (Fig. S8C, orange bar), suggesting that these bouts were due to activation of ChR2 by the imaging laser. Indeed, in the absence of two-photon scanning and holographic stimulation, we observed no spontaneous prey capture bouts (Fig. S8C, green). In summary, our holographic stimulation can evoke hunting, but two-photon scanning can also activate the *KalTA4u508* APN neurons to cause some prey capture bouts during the scanning period.

We observed that when our activation of the command-like neurons induced hunting, certain GCaMP-expressing cell bodies were activated. To identify neurons correlated with opto-hunting behavior, we constructed regressors for prey capture events, and defined neurons with $R^2 \geq 0.3$ as opto-hunting responsive. After activation of a small area within the APN (Fig. 5C, left panel, squares), we found cell bodies that were highly correlated with optogenetically-evoked eye convergence (Fig 5C, middle panel). These neurons also responded to our visual prey stimuli (Fig 5C, right panel), indicating that they are PRNs.

To determine whether some of the opto-hunting correlated neurons are *lhx9+*, we created masks of the brain regions labeled by the two lines (Fig. 5D, left, methods), and found that many of the opto-hunting neurons were located within the *lhx9* mask (Fig. 5D, middle), and these neurons were mostly located in the Thal, Pt, and NI (Fig. 5E). We also performed the experiment in larvae with only the *KalTA4u508* Gal4 driving ChR2 and GCaMP6s expression, and compared

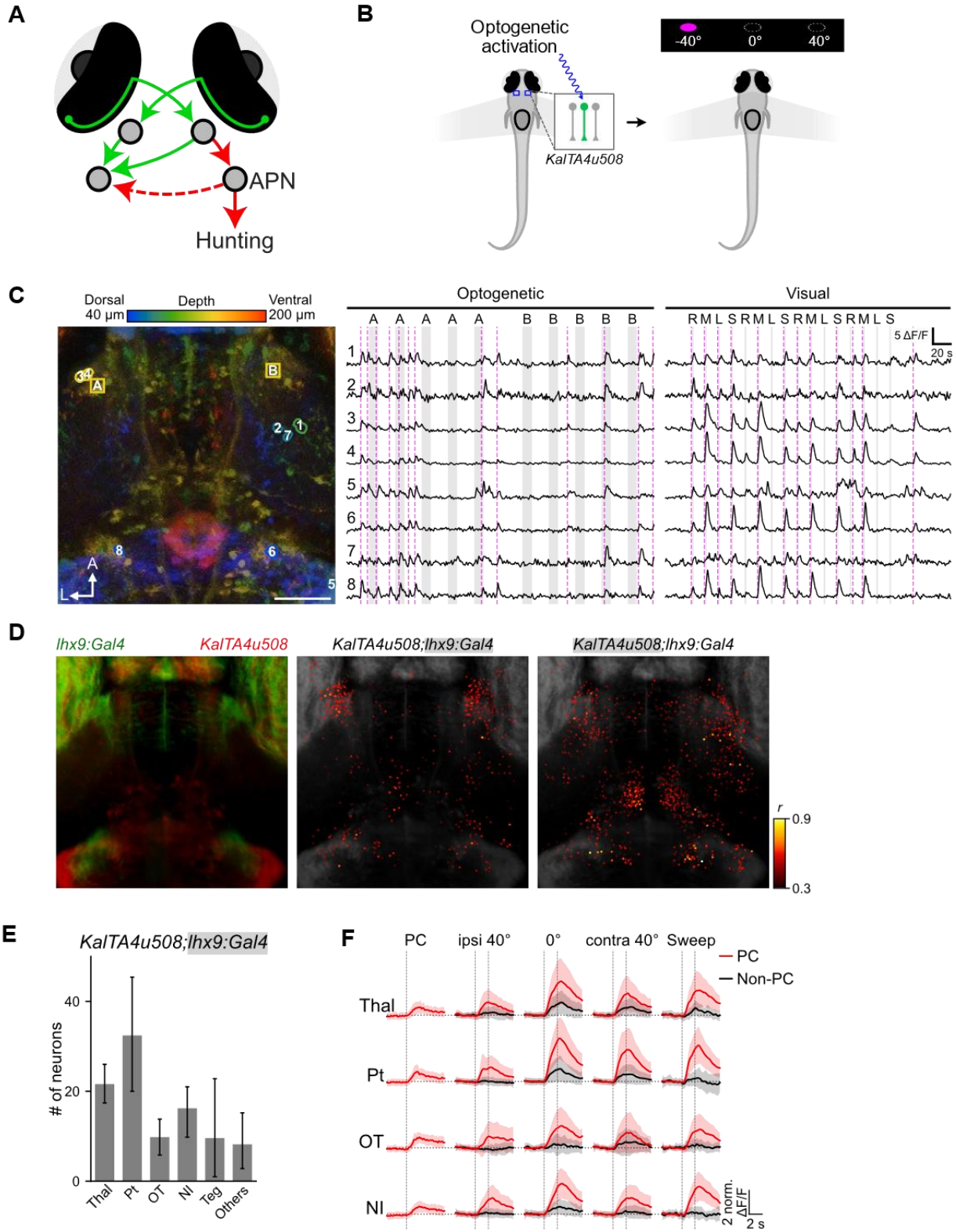
A
APN
Hunting
B
Optogenetic activation
-40°
0°
40°
KalTA4u508
C
Dorsal 40 µm
Depth
Ventral 200 µm
Optogenetic
Visual
A A A A A B B B B B
R M L S R M L S R M L S R M L S
5 ΔF/F
20 s
D
Ihx9:Gal4
KalTA4u508
KalTA4u508;Ihx9:Gal4
KalTA4u508;Ihx9:Gal4
r
0.9
0.3
E
KalTA4u508;Ihx9:Gal4
# of neurons
Thal
Pt
OT
NI
Teg
Others
F
PC
ipsi 40°
0°
contra 40°
Sweep
PC
Non-PC
Thal
Pt
OT
NI
2 norm. ΔF/F
2 s

Fig. 5. Optogenetically triggered hunting events activate *lhx9*+ neurons. (A) Model of motor signal from command-like APN neurons to bino-PRNs. **(B)** Schematic of sequential optogenetic activation and visual stimulation paradigm. *KalTA4u508*+ Pt neurons were holographically activated to trigger prey capture while performing 2-photon calcium imaging. After the opto-imaging session, prey stimuli were presented to record visual responses. **(C)** Left: example larva expressing GCaMP6s and ChR2 under control of the *KalTA4u508* and *lhx9* lines. Locations of the stimulation volume (square, 12 x 12 µm) and opto-hunting correlated neurons (circles). Middle: calcium traces of the top 8 opto-hunting correlated neurons in one fish. Grey shading represents stimulation of the left (A) or right (B) APN. Magenta dashed lines represent hunting onsets. Right: Responses to visual prey stimuli in the same 8 neurons. **(D)** Left: the *lhx9* (green) and *u508* (red) masks (left panel). Middle: opto-hunting neurons within the *lhx9* mask. Right: opto-hunting neurons in the *u508* mask. Dorsal view. n = 5 fish. **(E)** Average number of opto-hunting neurons in the *lhx9* mask in each brain region. Error bars indicate ±1 SD. n = 5 fish. **(F)** Visual responses of the opto-hunting neurons in different brain regions in prey capture (PC) and non prey capture (non-PC) trials. Solid lines and shaded regions represent mean and ±1 SD, respectively.

them to larvae with both Gal4s (Fig. S8D, right). We found that larvae with both Gal4s had more opto-hunting neurons in the Thal, Pt and NI (Fig. S8E, green) than those with *u508* only (red). This suggests that the *lhx9* neurons are downstream of the hunting motor command. To confirm that the opto-hunting neurons are PRNs, we next looked at the average population response to visual stimuli. We found that opto-hunting neurons in each area responded to prey stimuli, and the response was greater when these stimuli evoked hunting bouts (Fig. 5F). These results suggest that the lhx9-positive bino-PRNs are activated by the hunting command, possibly via corollary discharge.

To look more broadly at the whole population of neurons that receives hunting motor feedback, we performed similar optogenetic experiments with GCaMP expressed panneuronally. We co-expressed *elavl3:Hsa.H2B-GCaMP6s* with *KalTA4u508;UAS:ChR2(H134R)-mCherry*, and repeated the same experiment as in Fig. 5B with these fish. In this larger population, we found that the opto-hunting neurons shared a similar pattern in the brain with the bino-PRNs identified in Fig. 2H (Fig. S8F, left). In addition, a subset of these neurons were located within the *lhx9* mask (Figs. S8F, right, and S8G). Taken together, the two opto-hunting experiments give us genetic (*lhx9*), anatomical (Pt, Thal, NI regions) and functional (hunting enhanced PRNs) links between the opto-hunting neurons and the bino-PRNs. This suggests that the bino-PRNs are motor-enhanced at least partially because they receive hunting corollary discharge.

Coactivation of command-like neurons and lhx9 promotes prey capture forward swims.

We next sought to identify the functional role of the bino-PRNs in the lhx9 line by optogenetically activating them and observing the behavioral outcome. We first used an optic fibre to deliver 470 nm light to the whole brain to activate *KalTA4u508* neurons (Fig. 6A). As was previously reported, activating *KalTA4u508* neurons drove larvae to perform prey capture J-turns and forward swims(*18*). We then did the same experiment in larvae with Channelrhodopsin (ChR2) expressed in both the *lhx9* and *KalTA4u508* populations. In these double Gal4 larvae, we found that the optogenetically evoked prey capture bouts were significantly more symmetrical (Fig. 6B, Movie S2). Larvae bearing only the *lhx9* Gal4 also had higher bout symmetry (Fig. 6B). This higher symmetry could be due to a larger proportion of forward swim bouts, or a higher degree of symmetry within the forward swim bouts.

We then used a Support Vector Machine (SVM)(*17*) to classify the optogenetically induced bouts into different swim types, based on the bout asymmetry and maximum amplitude (Figs. 6C and 6D). We found that the addition of the *lhx9* population did result in more prey

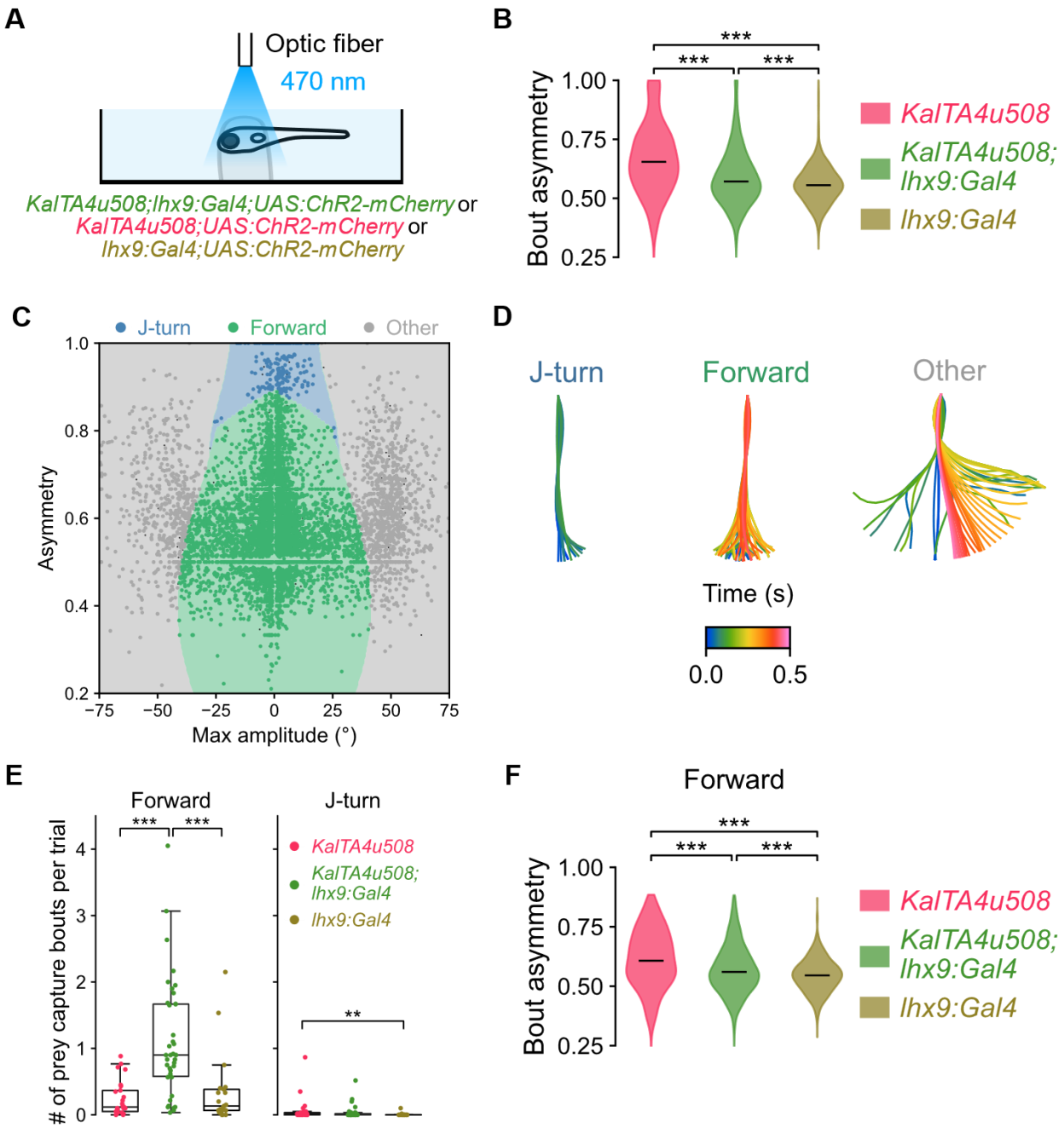

Fig. 6. Activation of *lhx9+* neurons preferentially evokes prey capture forward swims. (A) Schematic of the optogenetic activation experiment with larvae bearing one or both gal4 lines. **(B)** Bout asymmetry of opto-hunting bouts (defined by eye convergence) in the three genotypes (Kruskal-Wallis test followed by Dunn's test, *** $P < 0.001$). **(C)** The asymmetry and max amplitude values of all opto-hunting bouts of the three genotypes with J-turn, forward and other swim classification boundaries. **(D)** Example J-turn, forward swim and other bouts. **(E)** Number of J-turns and forward swims evoked by stimulation of the three genotypes of larvae (Kruskal-Wallis test followed by Dunn's test, ** $P < 0.01$, *** $P < 0.001$, otherwise $P > 0.05$). **(F)** Bout asymmetry of forward swims within each genotype (Kruskal-Wallis test followed by Dunn's test, ***$P < 0.001$).

capture forward swim bouts than the activation of *KalTA4u508* only (Fig. 6E). This may be due to the lower percentage of J-turns, higher prey capture rate, and larger number of bouts per trial (Figs. S9D-F). Activation of the *lhx9* line alone also produced forward swims (Fig. 6E), although the prey capture rate was lower (Fig. S9E). We also looked for differences in symmetry within forward swims, and found that the forward swims triggered by activation of *KalTAu508* had the highest asymmetry, those in the double Gal4 fish had lower asymmetry, and those with *lhx9* only had the lowest asymmetry (Fig. 6F). These results suggest that activation of bino-PRNs in the *lhx9* line preferentially triggers highly symmetrical forward swims.

Taken together, our findings suggest the bino-PRNs trigger prey capture forward swims, and that at the initiation of hunting, they receive an excitatory signal that the eyes have converged. We propose a model in which, during initial sighting of the prey, bino-PRNs are receiving prey sensory input from the contralateral retina as well as indirectly from the ipsilateral retina (Fig. 7A). When hunting is evoked, the prey sighting also activates the hunting command-like neurons in the APN, causing eye convergence and tail movement via outputs to the oculomotor nucleus (OMN) and hindbrain(*18*) (Fig. 7B). The motor signal may also be sent to the bino-PRNs as an indication that hunting initiation has occurred, and the eyes have converged. After the initial turn toward the prey and convergence of the eyes, the prey is now more likely to be in the binocular zone, and the next step in the hunting sequence is a forward swim. At this point, presence of the prey in the binocular visual field along with the hunting related signal can activate bino-PRNs to drive symmetrical approach swims toward the prey (Fig 7c).

Some steps within this model are supported by anatomical evidence. Within the pretectum, there is evidence for interhemispheric connections(*25*), which could allow for the activation of these neurons by prey seen by the ipsilateral eye. These projections innervate AF7 and project to the contralateral hemisphere, in the region of the Pt where we identified bino-PRNs (Fig. S10A). The function of the bino-PRNs in the Pt and Thal is unclear, but one output of the *lhx9+* neurons in the PT is to the ipsilateral hypothalamus (Fig. S10B)(*36*). Another anatomical question is how the bino-PRNs in Pt and Thal receive the motor signal. One possibility is that NI neurons project to these areas, and this is supported by the finding that *lhx9+* NI neurons project bilaterally to Pt and Thal (Figs. S10C and S10D)(*36*). Another question to be investigated is how the NI is activated by the hunting command. A recent finding identified a pathway from the APN to hindbrain medial rhombomere 5/6 (m-Rh 5/6) and showed that m-Rh5/6 neurons innervate both OMN and NI(*37*). Therefore, the m-Rh5/6 neurons could transmit a motor signal from the APN hunting command to the NI.

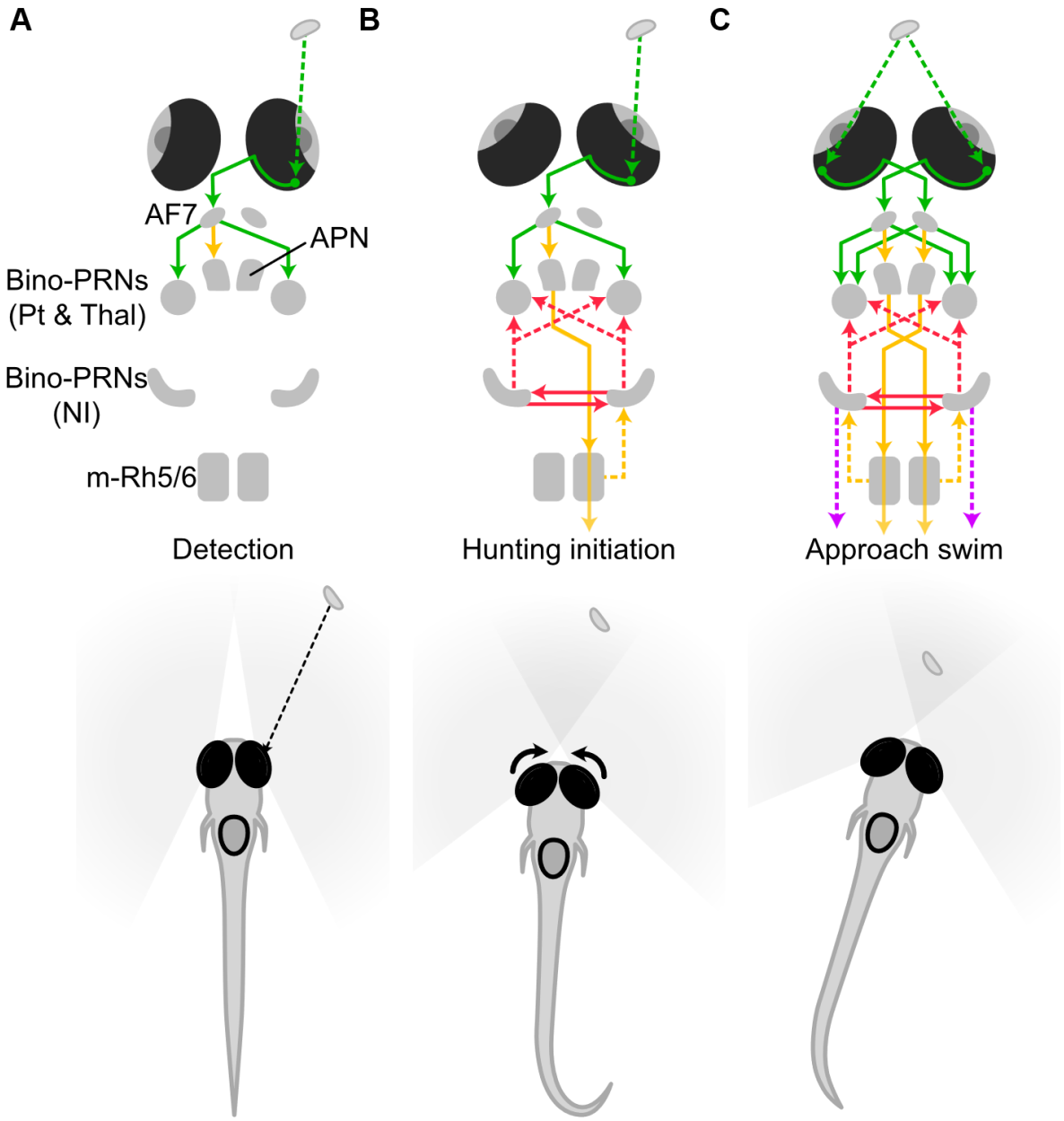

Fig. 7. Proposed circuit model of after prey detection bino-PRNs in mediating prey detection and promoting the behavioral transition to forward swimming upon sensory update and hunting action feedback. (A) Initial sighting of prey activates AF7 and bino-PRNs bilaterally. **(B)** Activation of command-like neurons in the APN initiates hunting and activates the bino-PRNs in the NI, possibly via the m-Rh5/6 region of the hindbrain. The NI has reciprocal connections with the opposite hemisphere and may broadcast the signal to the other bino-PRNs. **(C)** After the initial J turn, the presence of prey in the binocular zone plus the convergence signal maximally activates the bino-PRNs and triggers approach swims.

Discussion

Here, we identify binocular prey-responsive neurons in the zebrafish visual system, and find that these neurons are located primarily in the Pt, Thal, and NI. Notably, our bino-PRN population contained very few tectal neurons (Fig. 2H), although the tectum had the largest share of mono-contra PRNs (Fig. 2G). This absence is somewhat surprising given the importance of the tectum in prey capture behavior(*19*). It may be that while the tectum is important for some aspects of hunting, the Pt, Thal, and NI are the loci of excitatory binocular interactions. However, the tectum may receive inhibitory interhemispheric input, as shown by a recent study that identified a population of intertectal neurons that provide inhibitory input bilaterally to the OT(*21*).

Our imaging data suggested that bino-PRNs were more active in trials where hunting was initiated (Fig. S5). This effect could occur because the bino-PRNs are involved in generating the hunting motor command, or because they are receiving the hunting motor signal. Upon hunting initiation, larvae converge their eyes, creating a larger binocular zone in the frontal visual field, and prey in this zone will then evoke approach swims to bring the prey closer. It may be useful for the bino-PRNs to get a signal that hunting has been initiated, meaning that the larva has turned toward the prey and the eyes have converged, enabling both eyes to view the prey. This could be thought of as a locomotor state signal(*38*) or a corollary discharge which provides information on the expected location of the prey(*39*).

By activating a small region within the APN optogenetically, we were able to trigger hunting episodes, and show that the *lhx9+* PRNs, which are predominantly bino-PRNs, are activated by opto-hunting (Figs. 5, and S8). This means that they are receiving excitatory input as a consequence of hunting, which could be a corollary discharge. How could this input reach the bino-PRNs? The APN hunting command activates a region of the hindbrain called medial rhombomere 5/6, has projections to the oculomotor nucleus which also arborize in the nucleus isthmi(*37*). We hypothesize that these projections could evoke eye convergence via the oculomotor nucleus, and the input to the nucleus isthmi could be a convergence-related corollary discharge, which may activate bino-PRNs in the isthmi (Fig. 7A). The nucleus isthmi is well-positioned to broadcast the signal to other visual regions, as it provides input to the pretectum, thalamus, and tectum(*36*) (Fig. S10), and thus could activate bino-PRNs in those regions.

What is the function of the bino-PRNs, and why are they integrating binocular prey input with hunting state information? One possibility is that they could drive progression through the hunting sequence. Larvae typically do a J-turn upon initiation of hunting to orient toward the prey, and bring it into the binocular visual field. Then, they approach the prey with a more symmetrical forward swim (Fig. 7, lower panel). The bino-PRNs could be integrating binocular sensory information (prey can be seen by both eyes) with state information (hunting has been initiated) and driving forward swimming to approach the prey when these two conditions have been met.

As a first step to characterize the function of the bino-PRNs, we activated the *lhx9* population in conjunction with the command-like population, and found that the prey capture swims we evoked were more symmetrical than with the *KalTA4u508* line alone (Fig. 6). Our results are consistent with a previous study showing that activation of *lhx9* neurons drives slow swims, which may be forward swims(*36*). This suggests that one function of the *lhx9* population could be to promote prey capture forward swims. However, this may not be the only purpose of the bino-PRNs, as bulk activation of the entire population may miss some other functions. While the effect we saw resembled prey capture forward swims, it is also possible that some of the bino-PRNs are involved in determining the location of the prey or mediating strikes(*40*). Another caveat here is that although the majority of the *lhx9+* PRNs are bino-PRNs, there are other neurons in this line whose activation could contribute to the approach swims we see.

One additional function for bino-PRNs is suggested by anatomical data; *lhx9+* neurons in the Pt project to the hypothalamus(*36*) (Fig. S9B). This is reminiscent of the 119B pretectal neurons, which were previously shown to project to the lateral hypothalamus and play an important role in prey capture(*23*), although their binocular properties were not tested. It could be that these neurons integrate binocular prey sensory input with the signal that the eyes have converged to signal to the hypothalamus that prey consumption is about to occur, and thus modulate hunger/satiety state(*41*).

In conclusion, we identify a set of binocular neurons that respond specifically to prey stimuli. These neurons receive a hunting motor-related signal that the larva is in hunting mode and the eyes have converged, and integrate this with binocular prey input to drive symmetrical approach swims toward the prey. It is also possible that subsets of the population underlie other binocular functions, and with the localization of the binocular neurons and a Gal4 line that preferentially labels them, these possibilities can now be tested.

Materials and Methods

Animals

All procedures conformed to the guidelines by the animal ethics committee of HKUST. Animals were kept under a standard 14:10 light cycle at 28ºC. Zebrafish larvae carrying mutations in the *mitfa* allele (nacre) were used for all experiments(*42*). Larvae were kept in Danieau's solution, and fed with paramecia (*Paramecium multimicronucleatum*, Carolina Biological Supply Company) on 5 to 7 days post fertilization (dpf).

The following transgenic lines were used for this study: *Tg(atoh7:GAL4-VP16)s1992tTg*(*43*), *Tg(UAS:GCaMP6s)mpn101*(*44*), *Tg(elavl3:Hsa.H2b-GCaMP6s)jf5Tg* (*24*), *Tg(KalTA4u508)u508Tg*(*18*), *Tg(lhx9:Gal4VP16)mpn203*(*31*), *Tg(UAS:ChR2(H134R)-mCherry)mpn134*(*35*). For imaging of RGC axons and pan-neuronal imaging, For imaging of RGC axons and pan-neuronal imaging, *Tg(atoh7:Gal4VP16;UAS:GCaMP6s)* and *Tg(elavl3:Hsa.H2B-GCaMP6s)* fish were used, respectively. *Tg(lhx9:Gal4VP16;UAS:GCaMP6s)* and *Tg(KalTA4u508;UAS:GCaMP6s)* larvae were screened for binocular neurons. For two-photon optogenetic stimulation with calcium imaging experiments, *Tg(KalTA4u508;lhx9:Gal4VP16;UAS:GCaMP6s;UAS:ChR2(H134R)-mCherry), Tg(KalTA4u508;UAS:GCaMP6s;UAS:ChR2(H134R)-mCherry), Tg(lhx9:Gal4VP16;UAS:GCaMP6s;UAS:ChR2(H134R)-mCherry) and Tg(elavl3:Hsa.H2B-GCaMP6s; KalTA4u508;UAS:ChR2(H134R)-mCherry)* fish were used. For optic fiber stimulation experiments, *Tg(KalTA4u508;lhx9:Gal4VP16;UAS:ChR2(H134R)-mCherry), Tg(KalTA4u508; UAS:ChR2(H134R)-mCherry)* and *Tg(lhx9:Gal4VP16;UAS:ChR2(H134R)-mCherry)* fish were used.

Zebrafish Preparation

6-8 dpf larvae were embedded in 2% low melt agarose (Invitrogen) on 100 mm square (Thermo Scientific (cat# 109-17)) or 90 mm round (Thermo Scientific (cat#101VR20)) plastic petri dish. For eye-blocker experiments, the agarose surrounding the tail and in front of the head was removed by surgical blade (Paragon p303) to allow for tail and fin movements while eyes were kept in the agarose. Otherwise, both eyes and tail were freed. Fish were allowed to recover overnight prior to the experiment.

Eye-blocker design

Files describing the design of the eye-blocker are deposited in https://github.com/SemmelhackLab/eye-blocker-model. The components of the eye-blocker were fabricated using a 3D printer with black PLA plastic as the material. The eye-blocker was assembled from two arm parts and a body part. During imaging experiments, the tips of the eye-blocker arms were placed between the objective and the bottom of the fish arena. The height of

the tips was chosen to minimize the gaps at the top and the bottom without hindering the vertical movements of the objective. The body of the eye-blocker was attached to a 3-axes stage via an optical post. By controlling the movements of the 3-axes stage along the left-right axis of the fish, the arms of the eye-blocker could be moved to the position required for each ocular condition. The movements of the eye-blocker were visually guided by the live preview from the high-speed camera.

Lensectomy

At 6-7 dpf, larvae were embedded in 2% low melting agarose, and then the prep was immersed in 0.02% tricaine (MS-222 Sigma-Aldrich) to anaesthetize the larvae throughout the surgery. Lensectomies were performed with needle (Terumo 0.40 x 13mm). An incision was made in the transparent cuticle of the temporal side of the eye and lens was scouped out gently. Animals were then released from the agarose, allowed to recover overnight, and fed paramecia. The delensed larvae were re-embedded the next day (7-8 dpf), and tested the day after (8-9dpf).

Visual Stimulation

We adopted the spatial visual stimulator module (DLP® Light Crafter™ 4500 modified by EKB Technologies Ltd) to present stimuli as previously described(*45*). 385 nm "UV" LED (SOLIS-385C Thorlabs) and 590 nm "Red" LED (M590L4 Thorlabs) were used as the light sources. The Light Crafter (LCr) back projected to the 50 mm wide x 5 mm height Teflon fabric screen at 13.5 cm away. The screen was kept at 1 cm in front of the fish head.

Design of Visual Stimuli

Visual stimuli were created using PsychoPy. The prey-like circulating stimuli were UV dots, sized 4°×2°, moving in an elliptical path of 8°×4° at a speed of 2 Hz for 2 seconds on a dark background. The long axis of the dots was aligned to the movement direction. In the eye-blocking experiment (Figs. 1-4), the stimuli were presented at different positions, ranging from -50° (left) to 50° (right) in 10° steps. Stimuli on the left side moved counterclockwise, while those on the right moved clockwise. For the center azimuth (0°), we presented both counterclockwise and clockwise directions (indicated as -0° and +0°), resulting in 12 distinct stimuli. We randomly presented these 12 stimuli four times in each imaging session, with a 13 s interstimulus interval (ISI). We conducted two sessions for each eye condition, with at least a 5-minute pause between sessions, and followed a palindromic sequence for the eye conditions. The first stimulus in all experiments was shown 30 seconds after starting the two-photon scanning.

In the stimulus specificity experiment (Fig. S4), we conducted one imaging session each for left-eyed, right-eyed, and binocular conditions. The stimuli were the identical to those used in the eye-blocking experiment, except the background was red. After the sessions with the circulating dots, we presented a battery of eight additional types of stimuli under the binocular condition: darkening and brightening of the screen, leftwards and rightwards sweeping dots, leftwards and rightwards moving gratings, and slow and fast looming disks. The darkening and brightening stimuli changed the screen from red to black, or the reverse, over 10 seconds, with an ISI of 10 s. The sweeping dots have a size of 4°×2° and moved horizontally from -60° to 60°, or the reverse, over 2 s. The grating pattern was a sinusoid alternating between red and black with a cycle of 15° moving horizontally at 20°/s for 10 s. It remained visible but stationary during the 10-second ISI. The looming stimuli were dark circles that expanded from the screen's center at slow (l/v ratio = 0.25) and fast (l/v ratio = 0.125) speeds, with a 30-second interval between their initiations.

In the optogenetics imaging experiment (Fig. 5), we conducted a visual stimulation session after the optogenetic stimulation sessions. We used a sweeping stimulus in addition to the -40°, 0°, and 40° circulating stimuli. The sweeping stimulus was a 4°×2° UV dot moving horizontally from -60° to 60° over 2 s. The stimulus sequence of (-40°, 0°, 40°, sweep) was presented four times with an ISI of 13 s.

Behavioral Recording

Behavior was recorded at 200 Hz using a high-speed camera (PhotonFocus MV1-D1312-160-CL) at a resolution of 544×560 pixels, covering the entire fish and a small area in front to track the eye-blocker. Illumination was provided by an 850 nm infrared LED array beneath the fish arena, and an infrared band-pass filter on the camera lens blocked light from the two-photon laser.

Calcium Imaging

For the eye-blocker experiments, in-vivo calcium imaging was performed using a two-photon microscope (Nikon A1R MP+) equipped with a 25× water-immersion objective (Nikon CFI75 Apochromat 25XC W 1300, 1.1 numerical aperture). The excitation laser was calibrated to a wavelength of 1020 nm. An electrically tunable lens (Optotune EL-16-40-TC) was mounted behind the objective to enable multi-plane functional imaging. The imaged volume contains 9 planes with an average spacing of 15 µm between consecutive planes. Each plane was imaged at a resolution of 512×512 pixels (0.99 µm/pixel) at 3 Hz. Anatomical z-stacks were collected after the imaging sessions.

For the optogenetics experiments as in Fig. 5, a home-built two-photon light scanning microscope controlled by a C# based custom software is employed. The laser source is a Ti:Sapphire femtosecond laser (Chameleon Ultra II, Coherent) operating at 1020 nm wavelength for calcium imaging to reduce the crosstalk between GCaMP6s and ChR2. The laser beam first passes through the half-wave plate to adjust polarization direction. The laser beam with 2.2 mm in diameter (propagate a large distance from the laser source and expanded from 1.2mm) is expanded by a factor of ×7.14 through a 4f system (AC254-035-B-ML F = 35 mm, Thorlabs and AC254-250-B-ML F = 250 mm, Thorlabs) to full fill the ETL (EL-16-40-TC-NIR, Optotune AG), which is used for multi-plane functional imaging. Then a 4f system (AC254-200-AB-ML F = 200 mm, Thorlabs, and AC254-050-AB-ML F = 50 mm, Thorlabs) reduces the beam diameter to 4 mm to avoid overfilling the scanner mirror. A resonant scanner (CRS 8 kHz, Cambridge technology) for high-speed scanning is conjugated with a set of XY galvo scanners (6215H, Cambridge technology) by a 1:1 relay (AC254-100-AB-ML F = 100 mm, Thorlabs). Finally, two lenses (Scan lens SL50-CLS2 F = 50 mm, Thorlabs, and Tube lens TTL200MP F = 200 mm, Thorlabs) are used to correct the aberration and expand the laser beam to fill the objective back pupil (objective lens (20x, N.A. 1.0, XLUMPLFLN20XW, Olympus Corporation)). The ETL, resonant scanner, XY galvo scanners, and objective pupil plane are all conjugated. In the fluorescence collection path, a dichroic mirror (FF705-Di01-25*36, Semrock) is set between the tube lens and objective to reflect the fluorescence light, which then passes through two relay lenses (AC254-150-AB-ML F = 150 mm, Thorlabs and AC254-040-AB-ML F = 40 mm, Thorlabs) into the PMT (H11461-03, Hamamatsu). Two filters (FF03-525/50-25, Semrock, and FF01-600/52-25, Semrock) are installed on a flipper which can switch the filter to collect different fluorescence signals. Voltage signals are converted from PMT output current using a high-speed current amplifier (DHPCA-100, Femto) and digitized using an oscilloscope device (PCIe-8512H, ART technology).

Two-photon optogenetic stimulation

The laser source is a high-power ultrafast fiber laser (Toptica & FF Ultra 920). The laser beam first passes through the half-wave plate to adjust polarization direction. And then pass through a set of galvo scanner (6215H, Cambridge Technology). Then the light beam is expended by two lenes (AC254-50-AB-ML F = 50 mm, Thorlabs, and AC254-250-AB-ML F = 250 mm, Thorlabs) to fill the spatial light modulator (HSP1K-500-1200-PC8, Meadowlark Optics). Then the SLM is conjugated to the back focal plane of objective by a demagnify relay (AC508-250-AB-ML F = 250mm, Thorlabs, and AC254-150-AB-ML F =150 mm, Thorlabs). The photon stimulation light combines with imaging light by a polarized beam splitter (CCM1-PBS252/M; Thorlabs) between tube lens and dichroic mirror.

The hologram is calculated by compressive sensing weighted Gerchberg–Saxton algorithm(*46*) and loaded on SLM which controlled by a custom software on MATLAB. To compress the axial profile, a large beam diameter is applied to achieve an effective excitation NA (~0.5). Then by generating a spot array on each target, the target neuron can be fulfilled with a square of 10-12 um diameter and with an average power density of 0.15-0.3 mW/μm^2.

The spatial coordination between imaging light and photo stimulation light is calibrated before each optogenetics experiment. Two dark points are generated by photon bleaching a fluorescent microscope slide (FSK3, Thorlabs) for both imaging light and photo stimulation light. After calculating the displacement between them, a coordination shift is added to the hologram calculation.

During the two-photon optogenetics experiment, for each zebrafish larva, 6-8 sessions are conducted depending on the specific expression. For each session, a single pretectal *KalTA4u508* neuron is randomly selected according to mCherry expression and activated. Each session contains 5 trials, whereby each trial entails a 10-second duration of neuronal activation followed by a 30-second intertrial interval.

Single-photon optogenetic stimulation

Zebrafish larvae were placed in the petri dish and fixed with agarose. The eye and tail are freed by carefully cutting the agarose. An optical fiber, 200 μm in diameter, is held 5mm above the zebrafish larvae and guided the light from a blue light fiber-coupled LED (M470F4, Thorlabs). The irradiance at zebrafish larvae is 12-20 mW/cm^2 and adjusted by pulse-width modulation. Each trial contains a 2 s stimulation period and there is a 15 s interval between each trial. In total 60 trials are conducted for each fish. The whole petri dish is illuminated by an 850 nm LED array. Behavior is recorded at 100 Hz frame rate and analysed by custom Python software. The ChR2 expression is recorded after the experiment by two-photon imaging as a reference.

Behavioral Tracking

We tracked behavior using ztrack, a Python-based custom software. For eye tracking, we applied image thresholding around the fish's head, extracting the three largest contours from the image. The closest pair was identified as eyes, and the third as the swim bladder. Using the cv2.fitEllipse function from OpenCV, we fitted ellipses to these contours to find the centers and orientations of the eyes and swim bladder. We distinguished left from right eye based on the direction of the cross product between the vectors from the swim bladder to each eye. The fish's midline was defined as the line from the swim bladder's center to the midpoint between the eyes. The eye angles were computed as the angles between the major axes of the eyes and the midline. To track the tail, we used an iterative algorithm that traced 11 points along the tail, beginning at the most posterior point of the swim bladder. At each step, the algorithm identifies the next point on the tail by finding the brightest pixel among locations that were equidistant from the current point.

Behavioral Data Analysis

Eye convergence events were identified by detecting peaks in the vergence angle (left + right eye angle) after convolution with a step window function. Tail bouts were detected by thresholding the rolling standard deviation of tail angle over a 50 ms window. The asymmetry of each bout was calculated by first integrating the curvature over the last quarter of the tail and then determining the fraction of time points with curvature integrals that matched the sign of the bout's mean curvature. The maximum amplitude of tail bouts was measured by the peak tail tip angle. To classify bout types, we first manually labeled bouts as J-turns, forward swims, and others based on visual inspection of the videos. A Support Vector Machine (sklearn.svm.SVC) with a radial basis function kernel was trained to predict the bout type from the bout asymmetry and maximum amplitude with a leave-one-out cross validation accuracy of 86%.

Processing of Calcium Imaging Data

For each imaging plane, the non-rigid motion correction was performed using suite2p(*47*). In Fig. 1E, pixel intensities were preprocessed by z-score normalization across frames prior to analysis. In Fig. 1F, AF7 activity was calculated as the mean intensity of pixels within the manually annotated AF7 mask, followed by z-score normalization across time. The tuning curve in Fig. 1G was derived from the peak normalized AF7 activity within the stimulus interval.

For neuron-based analyses, the locations of regions of interest (ROIs) and their ΔF/F were extracted using the CNMF algorithm from the CaImAn package(*48*). The 10th percentile of a rolling 3-minite time window was used as the baseline for calculating ΔF/F. ROIs exhibiting a signal-to-noise ratio (SNR), as computed by CaImAn, below 2.5 were excluded from further analysis. The ΔF/F for each ROI was normalized by subtracting the mean and then dividing by the standard deviation obtained across all imaging sessions, followed by smoothing with a Gaussian filter ($\sigma = 0.33$ s).

Image Registration

Image registration was performed using the antsRegistration function from Advanced Normalization Tools (ANTs)(*49*) using parameters described(*50*). Anatomical z-stacks were registered to the templates provided by the mapZebrain atlas(*25*).

Assignment of Neurons to Anatomical Regions

For each region of interest (ROI), we calculated its x and y coordinates based on the center of mass of its spatial component. To determine the z coordinates, we identified the depth of each imaging plane by finding the z-stack layer that maximizes the Pearson correlation with the average fluorescence image of that plane. We then converted the 3D coordinates from the z-stack space to the atlas space using the function antsApplyTransformsToPoints. Lastly, we identified the anatomical region of each ROI by referencing annotated volume of the atlas at the transformed 3D coordinates.

Spatial *p*-value Analysis

For all maps showing the anatomical locations of functionally classified neurons from multiple fish, we retain only the neurons that demonstrate spatial co-localization across fish, as determined through the spatial *p*-value analysis described(*26*).

Regression Analysis

We generated stimulus regressors by convolving boxcar functions indicating stimulus presence with a calcium impulse response function (CIRF), which was modeled as a difference-of-exponentials(*51*). We conducted multiple linear regression analyses using sklearn.linear_model.LinearRegression. In the analysis in Fig. 2, we used 12 stimulus regressors (-50°, ..., -0°, +0°, ..., +50°) to model the ΔF/F for each ROI. Separate regression models were used for different ocular conditions, yielding one R^2 value per condition. For the analysis in Fig. 3, we concatenated the ΔF/F for each neuron across all ocular conditions. This concatenated data was then modeled as a weighted sum of 38 regressors, composed of 12 stimulus regressors for each of the three ocular conditions (left-eye (LE), right-eye (RE), and binocular) plus 2 motor regressors. For the analysis in Supplementary Fig. 4C, we used 8 stimulus regressors corresponding to the 8 stimulus types. An intercept term was included in all regression models.

Ocular Specificity Assignment

To categorize neurons into one of four ocular types in Fig. 2, we first compute the R^2 values for ipsilateral and contralateral conditions. For neurons in the left hemisphere, R^2_{ipsi} refers to R^2_{LE}, and R^2_{contra} refers to R^2_{RE}. For neurons on the right, these assignments are reversed. Neurons are then classified as follows: binocular neurons: both R^2_{ipsi} and $R^2_{contra} \geq 0.3$; mono-ipsi neurons: $R^2_{ipsi} \geq 0.3$ and $R^2_{contra} < 0.3$; mono-contra neurons: $R^2_{contra} \geq 0.3$ and R^2_{ipsi} le < 0.3. Neurons that do not fit any of these criteria are classified as "Other".

Hierarchical Clustering

In Fig. S4, we clustered neurons by their responses to the eight stimulus types using affinity propagation followed by hierarchical clustering, as descripted(*22*).

Identification of Motor Seed Neurons

We created simulated motor regressors for hunting towards the left and right by convolving Dirac delta functions, which mark the onsets of prey capture bouts to the left and right, with the CIRF. For each neuron, prey capture scores were determined using the formulas $\beta_L \cdot R^2$ and $\beta_R \cdot R^2$, where β_L and β_R represent the regression coefficients, and R^2 is the coefficient of determination from the linear regression model with the two simulated motor regressors. We identified the top 1% of neurons based on each score and applied spatial p-value analysis to retain only those neurons that were spatially co-localized across different fish. The neurons that selected neurons were primarily found in the pretectum and the intermediate medulla oblongata (IMO), with neurons located in the IMO displaying lower levels of sensory activity, thereby identifying them as the motor seed neurons. To calculate the final motor regressors for each fish, we averaged the ΔF/F of the top 5 motor seed neurons selected based on the scores.

t-SNE Dimensionalty Reduction and K-means Clustering

For the analysis in Fig. 3, we first reduced the 38 regression coefficients from the sensorimotor linear regression model to 35 by averaging the coefficients for the -0° and +0° stimulus. We then applied t-Distributed Stochastic Neighbor Embedding (t-SNE)(*52*) using sklearn.manifold.TSNE with perplexity = 100 to reduce the dimensionality to two dimensions. The t-SNE embedding was subsequently rotated to achieve symmetry. To group the neurons into distinct functional groups, we applied K-means clustering with a target of 20 clusters. Upon examining the coefficients among the clusters, we decided to merge 3 pairs of clusters that exhibited high similarity. This adjustment resulted in a total of 17 functional clusters.

Analysis of Imaging Data from Optogenetics Experiments

For the analysis in Fig. 5D, neurons were categorized as *lhx9:Gal4* or *KalTA4u508* depending on which corresponding z-scored fluorescence z-stack exhibited a higher z-scored fluorescence intensity at the neuron's location.

Quantification and Statistical Analysis

For each tuning curve, we determined the 95% confidence intervals through bootstrapping. We applied the Bonferroni method to adjust the *p*-values for multiple comparisons. For the box plots, the box spans from the first to the third quartile of the data, with the median marked by a line inside the box. The caps of the whiskers mark the most distant data points that are no more than 1.5 times the interquartile range away from the box. To estimate the 95% confidence intervals, we generate 1,000 bootstrap samples by resampling the data points with replacement. We then calculated their means and computed the 2.5^{th} and 97.5^{th} percentiles of these means.

References

1. A. Maier, M. A. Cox, J. A. Westerberg, K. Dougherty, Binocular Integration in the Primate Primary Visual Cortex. *Annu Rev Vis Sci* **8**, 345–360 (2022).
2. J. Cang, J. Fu, S. Tanabe, Neural circuits for binocular vision: Ocular dominance, interocular matching, and disparity selectivity. *Front Neural Circuits* **17**, 1084027 (2023).
3. J. D. Pettigrew, “The Evolution of Binocular Vision” in *Visual Neuroscience*, J. D. Pettigrew, K. J. Sanderson, W. R. Levick, Eds. (Cambridge University Press, illustrated, reprint., 1986), pp. 208–222.
4. V. Nityananda, G. Tarawneh, S. Henriksen, D. Umeton, A. Simmons, J. C. A. Read, A Novel Form of Stereo Vision in the Praying Mantis. *Current Biology* **28**, 588-593.e4 (2018).
5. R. C. Feord, M. E. Sumner, S. Pusdekar, L. Kalra, P. T. Gonzalez-Bellido, T. J. Wardill, Cuttlefish use stereopsis to strike at prey. *Sci Adv* **6**, eaay6036 (2020).

6. K. Allen, R. Gonzalez-Olvera, M. Kumar, T. Feng, S. Pieraut, J. L. Hoy, A binocular perception deficit characterizes prey pursuit in developing mice. *iScience* **25**, 105368 (2022).
7. K. P. Johnson, M. J. Fitzpatrick, L. Zhao, B. Wang, S. McCracken, P. R. Williams, D. Kerschensteiner, Cell-type-specific binocular vision guides predation in mice. *Neuron* **109**, 1527-1539.e4 (2021).
8. I. H. Bianco, A. R. Kampff, F. Engert, Prey capture behavior evoked by simple visual stimuli in larval zebrafish. *Front Syst Neurosci* **5**, 18496 (2011).
9. F. Kubo, B. Hablitzel, M. DalMaschio, W. Driever, H. Baier, A. B. Arrenberg, Functional Architecture of an Optic Flow-Responsive Area that Drives Horizontal Eye Movements in Zebrafish. *Neuron* **81**, 1344–1359 (2014).
10. A. L. Tesmer, N. P. Fields, E. Robles, Input from torus longitudinalis drives binocularity and spatial summation in zebrafish optic tectum. *BMC Biol* **20**, 24 (2022).
11. H. Fotowat, F. Engert, Neural circuits underlying habituation of visually evoked escape behaviors in larval zebrafish. *Elife* **12**, e82916 (2023).
12. B. W. Patterson, A. O. Abraham, M. A. MacIver, D. L. McLean, Visually guided gradation of prey capture movements in larval zebrafish. *Journal of Experimental Biology* **216**, 3071–3083 (2013).
13. S. A. Budick, D. M. O'Malley, Locomotor repertoire of the larval zebrafish: swimming, turning and prey capture. *J Exp Biol* **203**, 2565–2579 (2000).
14. D. S. Mearns, J. C. Donovan, A. M. Fernandes, J. L. Semmelhack, H. Baier, Deconstructing Hunting Behavior Reveals a Tightly Coupled Stimulus-Response Loop. *Current Biology* **30**, 54-69.e9 (2020).
15. C. K. Dowell, J. Y. N. Lau, I. H. Bianco, The saccadic repertoire of larval zebrafish reveals kinematically distinct saccades that are used in specific behavioural contexts. *bioRxiv*, 565345 (2023).
16. R. Blake, R. Fox, The psychophysical inquiry into binocular summation. *Percept Psychophys* **14**, 161–185 (1973).
17. J. L. Semmelhack, J. C. Donovan, T. R. Thiele, E. Kuehn, E. Laurell, H. Baier, A dedicated visual pathway for prey detection in larval zebrafish. *Elife* **3**, e04878 (2014).
18. P. Antinucci, M. Folgueira, I. H. Bianco, Pretectal neurons control hunting behaviour. *Elife* **8**, e48114 (2019).
19. E. Gahtan, P. Tanger, H. Baier, Visual Prey Capture in Larval Zebrafish Is Controlled by Identified Reticulospinal Neurons Downstream of the Tectum. *Journal of Neuroscience* **25**, 9294–9303 (2005).
20. P. M. Henriques, N. Rahman, S. E. Jackson, I. H. Bianco, Nucleus Isthmi Is Required to Sustain Target Pursuit during Visually Guided Prey-Catching. *Current Biology* **29**, 1771-1786.e5 (2019).
21. C. Gebhardt, T. O. Auer, P. M. Henriques, G. Rajan, K. Duroure, I. H. Bianco, F. Del Bene, An interhemispheric neural circuit allowing binocular integration in the optic tectum. *Nat Commun* **10**, 5471 (2019).
22. D. Förster, T. O. Helmbrecht, D. S. Mearns, L. Jordan, N. Mokayes, H. Baier, Retinotectal circuitry of larval zebrafish is adapted to detection and pursuit of prey. *Elife* **9**, e58596 (2020).
23. A. Muto, P. Lal, D. Ailani, G. Abe, M. Itoh, K. Kawakami, Activation of the hypothalamic feeding centre upon visual prey detection. *Nat Commun* **8**, 15029 (2017).
24. J. Freeman, N. Vladimirov, T. Kawashima, Y. Mu, N. J. Sofroniew, D. V Bennett, J. Rosen, C.-T. Yang, L. L. Looger, M. B. Ahrens, Mapping brain activity at scale with cluster computing. *Nat Methods* **11**, 941–950 (2014).

25. M. Kunst, E. Laurell, N. Mokayes, A. Kramer, F. Kubo, A. M. Fernandes, D. Förster, M. Dal Maschio, H. Baier, A Cellular-Resolution Atlas of the Larval Zebrafish Brain. *Neuron* **103**, 21-38.e5 (2019).
26. J. C. Marques, M. Li, D. Schaak, D. N. Robson, J. M. Li, Internal state dynamics shape brainwide activity and foraging behaviour. *Nature* **577**, 239–243 (2019).
27. A. Krauss, C. Neumeyer, Wavelength dependence of the optomotor response in zebrafish (Danio rerio). *Vision Res* **43**, 1275–1284 (2003).
28. T. Baden, Circuit mechanisms for colour vision in zebrafish. *Current Biology* **31**, R807–R820 (2021).
29. X. Chen, Y. Mu, Y. Hu, A. T. Kuan, M. Nikitchenko, O. Randlett, A. B. Chen, J. P. Gavornik, H. Sompolinsky, F. Engert, M. B. Ahrens, Brain-wide Organization of Neuronal Activity and Convergent Sensorimotor Transformations in Larval Zebrafish. *Neuron* **100**, 876-890.e5 (2018).
30. A. Muto, M. Ohkura, G. Abe, J. Nakai, K. Kawakami, Real-Time Visualization of Neuronal Activity during Perception. *Current Biology* **23**, 307–311 (2013).
31. D. Förster, I. Arnold-Ammer, E. Laurell, A. J. Barker, A. M. Fernandes, K. Finger-Baier, A. Filosa, T. O. Helmbrecht, Y. Kölsch, E. Kühn, E. Robles, K. Slanchev, T. R. Thiele, H. Baier, F. Kubo, Genetic targeting and anatomical registration of neuronal populations in the zebrafish brain with a new set of BAC transgenic tools. *Sci Rep* **7**, 5230 (2017).
32. M. Fukutomi, B. A. Carlson, A History of Corollary Discharge: Contributions of Mormyrid Weakly Electric Fish. *Front. Integr. Neurosci* **14**, 42 (2020).
33. G. B. Keller, T. D. Mrsic-Flogel, Predictive Processing: A Canonical Cortical Computation. *Neuron* **100**, 424–435 (2018).
34. B. Yogesh, G. B. Keller, Cholinergic input to mouse visual cortex signals a movement state and acutely enhances layer 5 responsiveness. *Elife* **12**, RP89986 (2023).
35. M. dal Maschio, J. C. Donovan, T. O. Helmbrecht, H. Baier, Linking Neurons to Network Function and Behavior by Two-Photon Holographic Optogenetics and Volumetric Imaging. *Neuron* **94**, 774-789.e5 (2017).
36. A. M. Fernandes, D. S. Mearns, J. C. Donovan, J. Larsch, T. O. Helmbrecht, Y. Kölsch, E. Laurell, K. Kawakami, M. dal Maschio, H. Baier, Neural circuitry for stimulus selection in the zebrafish visual system. *Neuron* **109**, 805-822.e6 (2021).
37. C. K. Dowell, "Motor Control of Rapid Eye Movements in Larval Zebrafish" (2023).
38. C. M. Niell, M. P. Stryker, Modulation of Visual Responses by Behavioral State in Mouse Visual Cortex. *Neuron* **65**, 472–479 (2010).
39. T. B. Crapse, M. A. Sommer, Corollary discharge across the animal kingdom. *Nat Rev Neurosci* **9**, 587–600 (2008).
40. B. Khan, O. mongkol Jaesiri, I. P. Lazarte, Y. Li, G. Tian, P. Zhao, Y. Zhao, V. D. Ho, J. L. Semmelhack, Zebrafish larvae use stimulus intensity and contrast to estimate distance to prey. *Current Biology* **33**, 3179-3191.e4 (2023).
41. C. L. Wee, E. Y. Song, R. E. Johnson, D. Ailani, O. Randlett, J.-Y. Kim, M. Nikitchenko, A. Bahl, C.-T. Yang, M. B. Ahrens, K. Kawakami, F. Engert, S. Kunes, A bidirectional network for appetite control in larval zebrafish. *Elife* **8**, e43775 (2019).
42. J. A. Lister, C. P. Robertson, T. Lepage, S. L. Johnson, D. W. Raible, nacre encodes a zebrafish microphthalmia-related protein that regulates neural-crest-derived pigment cell fate. *Development* **126**, 3757–3767 (1999).
43. F. Del Bene, C. Wyart, E. Robles, A. Tran, L. Looger, E. K. Scott, E. Y. Isacoff, H. Baier, Filtering of visual information in the tectum by an identified neural circuit. *Science (1979)* **330**, 669–673 (2010).
44. T. R. Thiele, J. C. Donovan, H. Baier, Descending Control of Swim Posture by a Midbrain Nucleus in Zebrafish. *Neuron* **83**, 679–691 (2014).

45. B. Khan, I. P. Lazarte, O. Jaesiri, P. Zhao, J. L. Semmelhack, Protocol for using UV stimuli to evoke prey capture strikes in head-fixed zebrafish larvae. *STAR Protoc* **5**, 102780 (2024).
46. P. Pozzi, L. Maddalena, N. Ceffa, O. Soloviev, G. Vdovin, E. Carroll, M. Verhaegen, Fast Calculation of Computer Generated Holograms for 3D Photostimulation through Compressive-Sensing Gerchberg-Saxton Algorithm. *Methods Protoc* **2**, 1–11 (2018).
47. M. Pachitariu, C. Stringer, M. Dipoppa, S. Schröder, L. F. Rossi, H. Dalgleish, M. Carandini, K. D. Harris, Suite2p: beyond 10,000 neurons with standard two-photon microscopy. *bioRxiv*, 061507 (2017).
48. A. Giovannucci, J. Friedrich, P. Gunn, J. Kalfon, B. L. Brown, S. A. Koay, J. Taxidis, F. Najafi, J. L. Gauthier, P. Zhou, B. S. Khakh, D. W. Tank, D. B. Chklovskii, E. A. Pnevmatikakis, CaImAn an open source tool for scalable calcium imaging data analysis. *Elife* **8**, e38173 (2019).
49. B. B. Avants, N. J. Tustison, G. Song, P. A. Cook, A. Klein, J. C. Gee, A reproducible evaluation of ANTs similarity metric performance in brain image registration. *Neuroimage* **54**, 2033–2044 (2011).
50. I. Shainer, E. Kuehn, E. Laurell, M. Al Kassar, N. Mokayes, S. Sherman, J. Larsch, M. Kunst, H. Baier, A single-cell resolution gene expression atlas of the larval zebrafish brain. *Sci Adv* **9**, eade9909 (2024).
51. M. A. Triplett, Z. Pujic, B. Sun, L. Avitan, G. J. Goodhill, Model-based decoupling of evoked and spontaneous neural activity in calcium imaging data. *PLoS Comput Biol* **16**, e1008330 (2020).
52. L. van der Maaten, G. Hinton, Visualizing Data using t-SNE. *Journal of Machine Learning Research* **9**, 2579–2605 (2008).

Acknowledgments

We thank Aristides Arrenberg and members of the Semmelhack lab for feedback on the manuscript.

Funding:
Hong Kong Research Grant Council grant 16103522 (J.L.S.)
Hong Kong Research Grant Council grant 16101221 (J.L.S)
Hong Kong Research Grant Council grant 16103118 (J.L.S.)
Hong Kong Research Grant Council grant 16102122 (J.Y.Q)
The Chau Hoi Shuen Foundation

Author contributions:
Conceptualization: GT
Methodology: GY, YH
Software: GY, TKCL
Formal Analysis: TKCL
Investigation: GT, TKCL, GY
Resources: GY,BK
Writing – Original Draft: GT, JLS
Writing – Review & Editing: all authors.
Supervision: JLS, JYQ
Funding Acquisition: JLS, JYQ

Competing interests: The authors declare no competing interests.

Data and materials availability: All data are available in the main text or the supplementary materials. Code is available at https://github.com/SemmelhackLab/binocular-paper

Supplementary Materials

Figs. S1 to S10.
Movies S1 to S2.